Cement and Concrete Research 141 (2021) 106330

Contents lists available at ScienceDirect

Cement and Concrete Research

journal homepage: www.elsevier.com/locate/cemconres

Modifying the pore size distribution in Fe-rich inorganic polymer mortars: An effective shrinkage mitigation strategy

G. Beersaerts [a,*], G. Ascensão [a,b], Y. Pontikes [a]

[a] KU Leuven, Department of Materials Engineering, Kasteelpark Arenberg 44, 3001 Leuven, Belgium
[b] Italcementi S.p.A, HeidelbergCement Group, via Stezzano, 87, 24126 Bergamo, Italy

ARTICLE INFO

Keywords:
Fe-rich slag
Alkali-activated materials
Inorganic polymers
Autogenous deformation
Drying shrinkage

ABSTRACT

Inorganic polymer (IP) binder is formed upon alkali-activation of Fe-rich (41 wt%) metallurgical slag leading to materials with mechanical properties comparable to ordinary Portland cement binders. Crack formation is reported in IPs, which can be related to volumetric stability, which is to date not thoroughly understood in IPs. This study determined the autogenous and drying shrinkage of IP mortars. Shrinkage mitigation strategies, such as the addition of 2-methyl-2,4-pentanediol (2MPL), blast furnace slag (GGBFS), and applying heat curing, were used separately or in combination. IP mortars exhibited autogenous expansion and high drying shrinkage. The addition of 2MPL led to a porosity increase, as air was entrained, decreasing the drying shrinkage with 64%. Additional heat curing had no effect on samples with 2MPL. Introducing GGBFS resulted in smaller pores, increasing drying shrinkage. Shrinkage in IP mortars is driven by its pore size distribution and higher shrinkage resulted in lower flexural strength.

1. Introduction

Fe-rich slags are by-products of the Cu, Pb and Zn metallurgical industry, which are currently either landfilled or used in low-value applications, such as filler material or in sand-blasting operations. The global production of Fe-rich slags from steel, copper and other non-ferrous metal production is estimated to be between 205 and 305 Mt./year [1], of which the Cu, Pb and Zn industry comprises a slag volume of 47–57 Mt./year [1]. The Cu and Zn slag volume reached in Europe alone an annual volume of around 6 Mt. [2,3]. Fe-rich slags are mainly amorphous, rich in FeO, SiO_2 and Al_2O_3, and are reactive upon alkali-activation [4]. When alkali-activated, the Fe-rich slag is dissolved, introducing mainly Fe, Si, Al, Mg and Ca ion species in the solution, first present as monomers and dimers. Once a level of saturation is reached, oligomers are formed, which further crosslink to polymers, and after some time a hard inorganic polymer (IP) binder is formed [5]. In this research, the name IP is chosen to refer to the formed binder, a name which is based on previous work on IPs made from Fe-rich slags [6]. The formation of an IP binder can open new perspectives on the slag valorization potential as IPs can obtain high mechanical properties and can, depending on the mix design, have a significantly lower environmental impact compared to ordinary Portland cement (OPC)-based materials [7]. This turns this rather underutilized material into an interesting alternative binder for construction materials.

In order to be an interesting binder for construction, the volumetric stability should be investigated, which can be driven by the pore size distribution in the monolith and depends on the type of binder formed. A volumetric instable binder can lead to the formation of cracks or the material can warp and curl. The latter can pose a problem in the installation or in the use phase of the material. Certainly, the formation of cracks can negatively affect the mechanical properties of the material and therefore it should be avoided. Although the volumetric stability in Fe-rich IPs is not thoroughly studied yet, some authors have described the presence of multiple micro-to macrocracks in the binder matrix [8–11]. Apart from IPs, the presence of cracks was also reported in binders formed from other alkali-activated materials (AAMs), such as alkali-activated metakaolin or ground granulated blast furnace slag (GGBFS) [12,13]. Cracks can be formed during shrinkage or expansion, when the stress generated from the length change, exceeds the strength of the binder. In isothermal conditions, different types of shrinkage can exist, such as chemical and drying shrinkage. Chemical shrinkage can be related to volume-reducing reactions, which takes place when the reaction products have a lower volume than the precursor. In IPs, the polymerization reactions result in a volume decrease and the release of

* Corresponding author.
E-mail address: glenn.beersaerts@kuleuven.be (G. Beersaerts).

https://doi.org/10.1016/j.cemconres.2020.106330
Received 29 August 2020; Received in revised form 10 November 2020; Accepted 8 December 2020
Available online 31 December 2020

water into the pores of the binder [5,14]. The chemical shrinkage includes the plastic deformation during the liquid stage of the mixture and the autogenous deformation is initiated during the setting when the material builds up strength to accommodate stress to counteract deformation. Autogenous deformation is related to self-desiccation shrinkage, which is generated in the pores of the matrix and is driven by the consumption of pore solution to form additional binding phases. This results in a loss of solution and a decrease in total pore volume, generating additional stress or capillary pore pressure [15,16]. Drying shrinkage takes place once water in the sample starts to evaporate. When water evaporates from the pores, an air-water interfacial tension is formed on the solid surface of the pore. The magnitude of stress generated in the pore is related to the pore size and water-air surface tension, according to the Young-Laplace equation [17]. This equation shows that pores of smaller radii develop a higher pore pressure [17,18]. The pore pressure is released when the surface tension decreases due to pore contraction, which results in shrinkage on macroscopic scale.

Mortars from alkali-activated fly ash, aluminosilicates and slags rich in FeO and CaO typically exhibit shrinkage, varying from 2 up to 8 mm/m at 28 days [19–22], which is significantly higher compared to OPC-based materials (± 1 mm/m) [23]. This indicates that shrinkage is a prominent problem in AAMs, which has to be overcome in order to be a potential replacement for OPC. The type of precursor and activator mainly defines the chemical structure and microporosity of the binder. The microporosity can be subdivided in three different pore regions depending on their pore diameter [24]. The smallest are the micropores (<1.25 nm), followed by the mesopores (between 1.25 and 25 nm) and the macropores (between 25 nm and 5000 nm) [24,25]. Pores with a diameter from 0.5 nm to 10 nm are related to the formation of the binder structure, while the meso-and macropores comprise the capillary pore region, which are the pores where capillary stress can be induced [18]. Binders from alkali-activated fly ash and GGBFS showed a higher drying and autogenous shrinkage compared to OPC-based mortars, up to 4 times, due to the higher mesopore volume (twice as high) in the binder [21]. The high autogenous shrinkage in alkali-activated GGBFS mortar can also be related to the used SiO_2/Na_2O molar ratio in the activating solution [26]. The drying shrinkage in alkali-activated GGFSB is found to be dependent on the relative humidity to which the sample was exposed, which determined the pore size distribution, the interaction within the binder and the binder rearrangement [27]. When replacing GGBFS with fly ash, the mesopore volume decreased, resulting in a decrease in shrinkage [21]. Introducing metakaolin in alkali-activated GGBFS resulted in a decrease in autogenous shrinkage, implying that the binder chemistry and pore size distribution can be tailored by a proper selection and combination of different precursors [28]. Furthermore, literature reported that the slags' reactivity, of slags rich in FeO and with various amounts of CaO, can determine the magnitude of autogenous length change [19].

Another way to reduce shrinkage is the use of shrinkage reducing agents (SRAs) [29], which were initially developed for OPC-based materials. Reactive SRAs, such as periclase, anhydrite, lime and gypsum modify the chemical composition of the binder by altering the type of hydration reactions and by promoting the formation of expansive phases. Such a shrinkage mitigation strategy is not only effective in OPC-based materials but was also reported in binders formed from AAMs [27,29–33]. Also non-reactive, organic-based SRAs exist and can be used to alter the pore size distribution and the water surface tension in the mixture [34]. In cementitious binders, non-reactive SRAs, such as superplasticizers for instance, are used to decrease the water content, and consequently decreasing the drying shrinkage, without imposing a loss in flowability. AAMs, however, consist of a higher alkaline environment and a different zeta potential between the plasticizers and the precursor particles compared to OPC-based binder. Consequently, superplasticizers, such as polycarboxylate, melamine-based and vinyl copolymer admixtures, are less effective or they even break down and don't work [35–37]. Some non-reactive SRAs are alkali-resistant, such as polyethylene glycols and polypropylene glycols, and are reported to be effective pore size modifiers in alkali-activated GGBFS [33,38,39]. Another non-reactive SRA reported in literature is 2-methyl-2,4-pentanediol (2MPL), of which 1 wt% addition decreased drying shrinkage by 80% in an alkali-silicate-activated GGBFS due to the delay in reactivity which resulted in coarser pores [40].

Heat curing is reported in literature as a way to decrease shrinkage in alkali-activated fly ash and GGBFS as it decreased the total porosity [41] and improved the strength of the binder [42]. *Ascensão* et al. (2019) stated that heat curing of Fe-rich IP mortars decreased the total porosity and reduced the total shrinkage by 30% as it accelerated the formation of a stronger binder which can accommodate higher stresses during drying [19].

The effectiveness of the aforementioned shrinkage mitigation strategies and its associated driving mechanisms are to the best of our knowledge not investigated for Fe-rich IP mortars. This work aims to explore different ways to modify the pore size distribution of the final IP mortar, by introducing a non-reactive organic SRA, by the addition of GGBFS and by applying heat curing to obtain a volumetrically-stable IP. As non-reactive SRA 2MPL was chosen (0–3 wt% of precursor) and the optimum dosage was found with respect to shrinkage reduction. IPs were produced from Fe-rich slag and partially replaced by GGBFS in an attempt to modify the binder chemistry and its pore size distribution. Additionally, each of these IP mortars, with or without 2MPL or GGBFS, underwent ambient and heat curing (60 °C). The pore size distribution, the flexural and compressive strength at 28 days, and the microstructure were assessed for each mortar formulation.

2. Materials and methods

2.1. Precursor characterization

Two types of slag were used in this study, an Fe-rich slag (SL), a byproduct from the Cu industry and used as main precursor, and ground granulated blast furnace slag (GGBFS), provided by Ecocem. The received SL was milled to a fine powder with an attritor mill (1S Wiener). The bulk chemical compositions of SL and GGBFS were analysed by X-Ray Fluorescence (XRF, spectrometer PW 2400, Philips). Samples were prepared to identify the mineralogical composition of SL and GGBFS by blending SL and GGBFS with the internal standard, ZnO, with a McCrone micronizing mill, and using ethanol (>99% pure) and ZrO_2 beads as grinding and milling agent. The mineralogical composition of SL and GGBFS was analysed using X-Ray Diffraction (D2 Phaser XRD, Bruker) measuring in a range of 5° to 70° 2θ at a voltage of 30 kV and a current of 10 mA. Mineralogical identification was conducted using Diffrac EVA and quantification was carried out using the Rietveld algorithm and the software TOPAS Academic V5. The Fe^{2+} content was determined by performing a redox titration. 0.1 g of SL was dissolved in a Teflon beaker with a sulfuric and fluoric acid solution (20 ml demi water with 4 ml 50 wt% H_2SO_4 and 2 ml 50 wt% HF), while stirring with magnetic stirrers for 2 h long in an Argon environment. After the 2 h, the HF was neutralized and 2.5 g H_3BO_3 and 5 ml 40 wt% H_2SO_4 was added, followed by the addition of 1 ml 0.0001 M ferroine indicator to indicate the Fe oxidation state. Afterwards, the dissolved sample with redox indicator was titrated with 0.01 M $Ce(SO_4)_2$ until the equivalence point was reached. Based on the titrated volume and concentration of $Ce(SO_4)_2$ the Fe^{2+} content of the sample was calculated and the Fe^{2+}/Fe^{3+} mass ratio was identified [43]. The particle size distribution of SL and GGBFS was measured by laser diffraction (LS 13320, Beckman Coulter) in a dry state. The density of SL and GGBFS was measured by a gas pycnometer according to ASTM-B417-64 and the specific surface area was measured by the Blaine method according to EN 196-6.

2.2. Inorganic polymer synthesis

The mix design for producing the inorganic polymer (IP) pastes is

shown in Table 1. A potassium-silicate activating solution over slag (GGBFS + SL) mass ratio of 0.38 was used as preliminary experiments have shown that a good flow was obtained with this ratio. The potassium-silicate solution, containing a SiO_2/K_2O molar ratio of 1.7 and 65 wt% H_2O, was prepared at least 24 h prior to the IP production. The 2-methyl-2.4-pentanediol (2MPL) was added to the activator prior to the paste preparation. The paste was prepared by mixing the precursor and the activating solution for 1 min in a 5 L Hobart at 139 rpm. IP mortars were produced by using the mix design in Table 1 and by using sand (Sibelco, M31) with a sand to slag mass ratio of 1.5, which was added to the IP paste during mixing (139 rpm) within 1 min. The complete mixture was mixed for another 30 s at 285 rpm. After mixing, the mortar was cast in 4 × 4 × 16 cm^3 moulds and 60 jolts were performed. The IP mortars were coded according to the content of 2MPL, GGBFS and curing conditions, as shown in Table 1. An amount of 0, 1, 2 or 3 wt% of 2MPL was used, which is named respectively, 0-2MPL, 1-2MPL, 2-2MPL or 3-2MPL. When 15 wt% of the SL was replaced by GGBFS, "15G" was added to the sample notation. All samples were cured at 20 °C and 100% RH for 24 h. Afterwards, the samples were demoulded and samples 3-2MPL-H, 0-2MPL-15G-H and 3-2MPL-15G-H were wrapped in plastic foil for additional heat curing for 3 days at 60 °C and 100% RH. The heat-cured samples were noted with a 'H' at the end of the sample notation, while the ambient cured samples were noted with a 'A'.

2.3. Calorimetry

The reaction kinetics of the pastes 0-2MPL-A, 3-2MPL-A and 0-2MPL-15G-A (Table 1) were investigated by isothermal calorimetry (TAM Air, TA Instruments) at 20 °C for 24 h to identify the influence of the additions on the rate and total heat flow produced. The pastes were mixed inside the calorimeter by using admix ampoules.

2.4. Autogenous deformation, drying shrinkage, weight loss and mechanical strength

IP mortars (mix design see Table 1) were produced and were cast within 4 min in a flexible corrugated tube for measuring the autogenous deformation. During filling, the tube was vibrated to obtain optimal compaction. Once the tube was filled it was sealed and the plastic and autogenous shrinkage was measured with a linear variable differential transformer according to ASTM C 1698 for 7 d at constant temperature of 20 °C [44]. To conduct drying shrinkage measurements, the IP mortars were cast in 4 × 4 × 16 cm^3 moulds with inserted pins and cured in sealed conditions for 24 h at 20 °C (EN 12617-4). After 24 h, the samples were demoulded and the initial length and weight of the samples were measured. Afterwards, samples 3-2MPL-H and 0-2MPL-15G-H were wrapped in plastic foil and heat-cured, while for samples 0-2MPL-A, 1-2MPL-A, 2-2MPL-A, 3-2MPL-A, 0-2MPL-15G-A, 3-2MPL-15G-A the shrinkage behaviour and weight loss were measured at 20 °C and 50% RH (Table 1). After heat curing, samples 3-2MPL-H and 0-2MPL-15G-H were unwrapped, kept at 20 °C and 50% RH, and the drying shrinkage and weight loss were also measured till 28 d. The shrinkage is given in units of mm/m, where 1 mm/m = 1000 με. The 28 d flexural and compressive strengths of the mortars were determined using an Instron 5985 at a constant displacement rate of 0.5 mm/m for flexural and 2 mm/m for compression testing (EN 196-1). Duplicates were made to investigate the variation in autogenous shrinkage, drying shrinkage, weight loss and mechanical strength.

Table 1
The mix design of each sample and its curing condition.

Sample name/ amount (g)	SL	GGBFS	Solution	2MPL	Curing temperature (±1 °C)
0-2MPL-A	100	0	38	0	20 °C
1-2MPL-A	100	0	38	1	20 °C
2-2MPL-A	100	0	38	2	20 °C
3-2MPL-A	100	0	38	3	20 °C
3-2MPL-H	100	0	38	3	60 °C
0-2MPL-15G-A	85	15	38	0	20 °C
0-2MPL-15G-H	85	15	38	0	60 °C
3-2MPL-15G-A	85	15	38	3	20 °C
3-2MPL-15G-H	85	15	38	3	60 °C

2.5. Water absorption and mercury intrusion porosimetry

IP mortars (2 × 2 × 2 cm^3 cubes) were made of each formation (Table 1) to assess the porosity and pore size distribution at 28 d. Prior to each porosimetry test, the samples were dried for 24 h in an oven at 50 °C and afterwards vacuum-dried for another 24 h to ensure that any residual moisture in the pores was removed which is desired to obtain proper porosimetry results. The water absorption under vacuum was performed according to EN 1936 [45]. The pore size distribution was further investigated by mercury intrusion porosimetry (MIP) with a Micrometrics Poresizer 9310, which has a measurement range from 5 nm to 500 μm. Porosimetry measurements were not possible in the micropore region (<1.25 nm) [24] due to technical limitations. Low-pressure Hg intrusion from 0 to 30 psi was performed first to intrude the large macropores. Afterwards, Hg was introduced into the sample at high pressure from 30 to 30,000 psi to intrude the macro-to mesopores of the material. The relative porosity for each pore size could be calculated with the Young-Laplace equation [17].

2.6. Scanning electron microscopy (SEM)

Fragments of IP mortar samples 3-2MPL-A, 0-2MPL-15G-A and 3-2MPL-15G-A (Table 1) were polished, and coated with a 5 nm Pt layer, for characterization of the microstructure with a Philips XL30 FEG Scanning Electron Microscope (SEM). In order to obtain high-resolution backscattered electron (BSE) images, a 20 kV beam with a working distance of 10 mm was used. Qualitative point analyses were performed with an energy dispersive x-ray detector (EDX) to determine the chemical composition of certain phases situated in the binder.

3. Results and discussion

3.1. Precursors characterization

The chemical bulk composition of SL and GGBFS is shown in Table 2. SL comprised of Fe_2O_3 and FeO which is, respectively, 2.7 wt% and 37.6 wt% over total content of solids (Fe^{2+}/Fe^{3+} mass ratio 14.0). SL is 92.7 wt% amorphous, as indicated by the hump between 20°-40° 2θ in the X-ray diffractogram in Fig. 1. The peaks at 31° and 36° 2θ were identified as spinel (6.7 wt%) and the peak at 45° 2θ was identified as metallic Fe (0.7 wt%). The GGBFS is almost fully amorphous (>95%) as indicated by the pronounced hump between 20° and 40° 2θ in Fig. 1. The specific density, specific surface area and particle size distribution of SL and GGBFS are given in Table 3.

3.2. Calorimetry

The heat flow development of 0-2MPL-A, 3-2MPL-A and 0-2MPL-15G-A was measured to investigate if 2MPL and GGBFS would affect the reactivity of the IP pastes (Fig. 2A and B). Each heat flow curve showed two peaks, of which the first peak is the initial reaction peak due to wetting and initial dissolution of the slag. The second heat flow peak can be related to the binder formation and its acceleration period might provide an indication for the setting time [6,46]. When 15 wt% of the SL was replaced by GGBFS (0-2MPL-15G-A), the reaction kinetics were accelerated, resulting in a higher and earlier heat flow peak compared to 0-2MPL-A. The addition of 2MPL did not influence the reactivity (Fig. 2A) and both heat flow peaks, 0-2MPL-A and 3-2MPL-A, took place

Table 2
The bulk chemical composition of SL and GGBFS, with FeO* present as FeO and Fe_2O_3 and Fe as metallic Fe.

(wt%)	FeO*	Fe	SiO_2	CaO	Al_2O_3	ZnO	MgO	Cr_2O_3	P_2O_5	Na_2O	SO_3	Other
SL	40.3	0.7	32	4	11	2	1	2	2	2	/	3
GGBFS	0.4	/	33	42	12	/	8	/	/	0.3	2.5	2.2

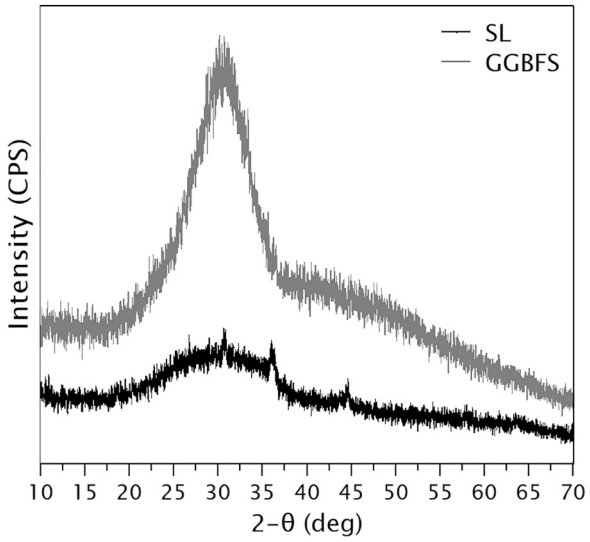

Fig. 1. The X-ray diffractogram of SL and GGBFS.

Table 3
The bulk chemical composition of SL and GGBFS.

Precursor	Relative density (g/cm^3)	Specific surface area (cm^2/g)	Particle size distribution (μm)		
			D_{10}	D_{50}	D_{90}
SL	3.4	7700	1.2	4.8	17.2
GGBFS	2.9	4500	2.9	12.5	31.4

5 h after mixing. These results differ from the results reported by *Bílek* et al. (2016) who concluded that the addition of 2MPL in alkali-activated GGBFS mortars resulted in a delay of the reaction kinetics [40]. The reaction products in IP systems are known to be different from alkali-activated GGBFS, of which the latter forms C-(A)-S-H types of binder products [22], which can explain why a delay was not recorded for the IP pastes in this work.

The cumulative heat flow results in Fig. 2B shows that the GGBFS-containing paste had an exponential increase in cumulative heat flow during the first 4 h, which evolved afterwards towards a continuous increment. This is not the case for the samples 0-2MPL-A and 3-2MPL-A, which showed an exponential increase in cumulative heat flow after 5 h. The accelerated reactivity of 0-2MPL-15G-A is explained by the higher reactivity of GGBFS [47,48] compared to SL, resulting in faster dissolution of Ca, Al, Si and Mg species, leading to a faster precipitation of a binder. The higher total reactivity of 0-2MPL-A and 3-2MPL-A compared to 0-2MPL-15G-A can be explained by the higher surface area of SL. Furthermore, the early-formed binder in 0-2MPL-15G-A, mostly originating from the dissolution of GGBFS, potentially covers the partially reacted GGBFS particles and the less reactive SL particles, inhibiting further dissolution and reaction [49].

3.3. Autogenous shrinkage

The corrugated tube experiments showed for sample 0-2MPL-A shrinkage during the first 24 h after mixing (Fig. 3A). The transition from plastic to autogenous shrinkage took place after 5–6 h which can be identified as the decrease in shrinkage rate [50]. The plastic shrinkage behaviour ceased when the setting time was reached, which is indicated by the change in curve gradient [50]. The initial setting time, and thus also the change in gradient, roughly corresponded with the acceleration period of the main reaction peak in Fig. 2A, indicating that the setting time is likely situated around 5–6 h [46]. After this transition period, the length change in hardened state was measured [50]. The plastic and autogenous shrinkage is followed by an expansion event (6.4 mm/m), which lasted for 3 h and took place after the heat flow peak, and is thus considered post setting.

Sample 0-2MPL-15G-A did not show such an expansion event, only chemical shrinkage was measured with a transition from plastic to autogenous shrinkage (setting time) after 1 h (Fig. 3A). This transition coincided also with the heat flow peak. The absence of expansion in 0-2MPL-15G-A can be related to the accelerated reactivity due to the addition of GGBFS (see 3.2. Calorimetry), resulting in the early precipitation of a different binder and preventing that the expansion could take place. The total plastic shrinkage of sample 0-2MPL-A (1.1 mm/m) was 2.7 times higher compared to 0-2MPL-15G-A (0.4 mm/m).

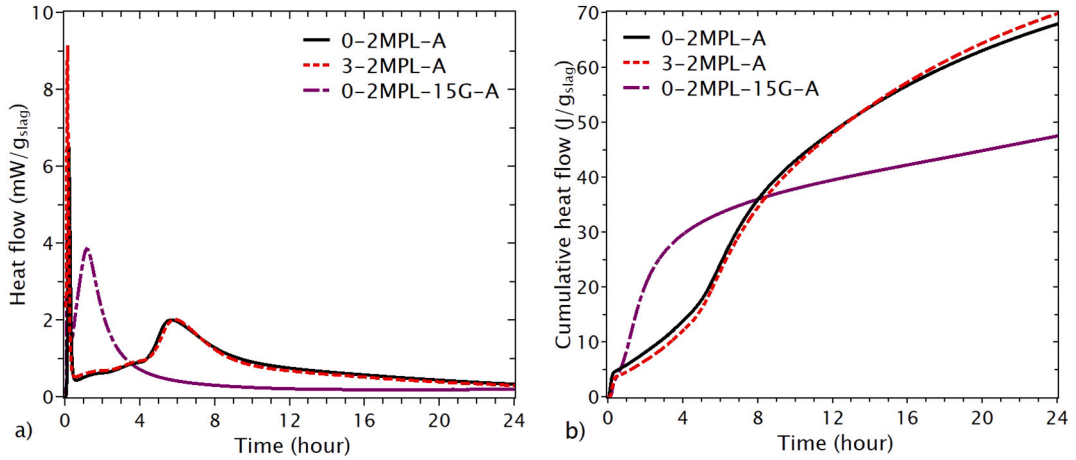

Fig. 2. The calorimetry results of 0-2MPL-A, 3-2MPL-A and 0-2MPL-15G-A: (a) heat flow and (b) cumulative heat flow during the first 24 h.

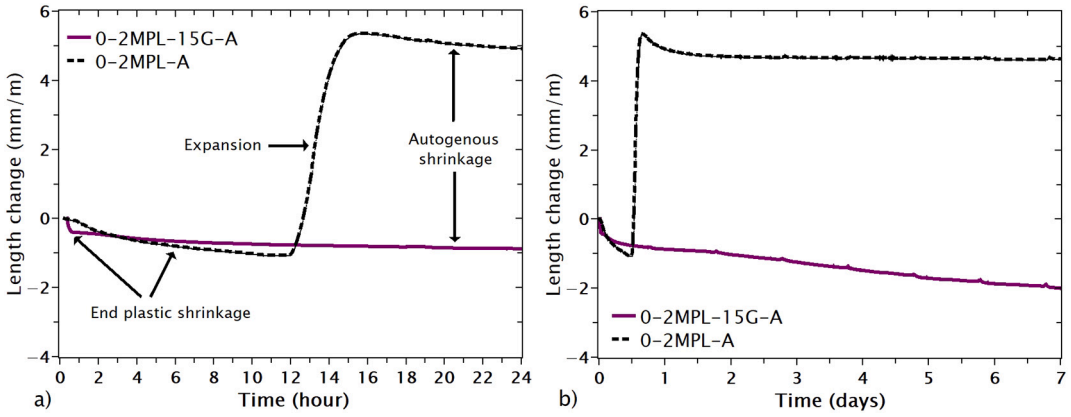

Fig. 3. The autogenous length change of 0-2MPL-A and 0-2MPL-15G-A: (a) during the first 24 h; (b) for 7 days long.

Several options are feasible to explain the expansion event. The first option is related to the formation of the Fe^{2+} trioctahedral layers, explained in previous research [51], which is suggested to take place during polymerization only, and coincides with the expansion event. The formation of these Fe^{2+} trioctahedral layers (similar in structure to $Fe(OH)_2$) might lead to a volume increase [52]. Based on these reasons, there might be an indication that the formation of such binder can affect the volumetric stability. The second plausible option for explaining the expansion is related to the oxidation of metallic Fe. In order to prove whether or not the metallic Fe particles contribute to the expansion, some additional autogenous deformation experiments were conducted with another slag that did not have metallic Fe particles and consisted of an Fe^{2+} proportion similar to SL. The autogenous deformation of the slag without metallic Fe did not show any expansion. A second autogenous deformation experiment was conducted with this slag and 1.7 wt% (over slag) of metallic Fe powder. The introduction of metallic Fe powder resulted in a decrease in plastic shrinkage and a small expansion event around 2 h post mixing, which coincided with the transition from plastic to autogenous deformation. The measured expansion was much smaller compared to the expansion obtained from SL in current research, which can be related to the difference in morphology and the added metallic Fe powder was probably coarser compared to the metallic particles in SL, offering less surface to oxidise. In previous research, the authors suggested that the expansion can be related to the Fe, which can affect the crystallization processes and the formed binder [19]. Probably, the expansion is caused by an interplay of several effects, such as the formation of Fe^{2+} trioctahedral layers for example. In general, no conclusive explanation for the expansion event can be given with the techniques carried out in this research.

Fig. 3B shows the 7 d autogenous deformation of 0-2MPL-15G-A and 0-2MPL-A. The autogenous shrinkage post-expansion in 0-2MPL-A evolved after two days to a plateau of 4.6 mm/m with a total shrinkage of 0.7 mm/m. The autogenous shrinkage of 0-2MPL-15G-A did not evolve towards a plateau value but continued to increase, with a total value of 2.0 mm/m at day 7, implying that the total autogenous shrinkage of 0-2MPL-15G-A is higher than 0-2MPL-A. The large autogenous shrinkage of 0-2MPL-15G-A can be explained by the formation of a different binder due to the introduction of GGBFS. The pore refinement might can be related to possible hydration reactions, which can cause self-desiccation [16]. In IP mortars without GGBFS water is most likely not chemically bound, and thus self-desiccation reactions might not occur, which would explain the low autogenous shrinkage. This statement was supported by *Pacheco-Torgal* et al. (2015), stating that, when the water is not chemically bounded, the water is most likely situated in the micro to macropores, of which the latter are entangled in the binder structure of the alkali activated material [14,22]. Thermal analysis of IP samples showed that, unlike hydrated cements, the water in IP samples is mainly "free" water and thus not bonded in the structure [8]. Research is being conducted to identify how the water is exactly structured in the IP binder.

3.4. Drying shrinkage and weight loss results

Once all IP mortars were exposed to dry conditions (50% RH), a strong increase in shrinkage was observed during the first 7 days and afterwards evolved to a plateau value (Fig. 4A and B). Sample 0-2MPLA exhibited the highest shrinkage, 5.1 ± 0.2 mm/m, at 28 days, followed by 1-2MPL-A (4.7 ± 0.01 mm/m). A significant decrease in shrinkage of 62% was measured when 2MPL was increased from 1 to 2 wt% (2-2MPL-A). Further increasing the dosage of 2MPL from 2 to 3 wt% (3-2MPL-A) resulted in only a small decrease in shrinkage to 1.4 ± 0.1 mm/m. Additional heat curing did not significantly reduce shrinkage in sample 3-2MPL-H. The weight loss was proportional to the 2MPL dosage, of which 0-2MPL-A had the lowest and 3-2MPL-A had the highest weight loss, 3.6 and 5.2%, respectively (Fig. 4B). The weight loss was significant during the first 7 days and seem to follow a similar behaviour as the shrinkage, proving that the shrinkage is driven by drying. The weight loss of 3-2MPL-H at 28 days was 14% lower compared to 3-2MPL-A indicating that heat curing can accelerate the reactivity resulting an increased amount of closed pores. Literature reports that hydration reactions do not take place in alkali-activated aluminosilicates and consequently water is not chemically bonded to the structure of the matrix [14,22]. This can also be the case for Fe-rich, low-Ca IPs, like the ones formed in current research, implying that the decrease in weight loss is likely not attributed to hydration reactions.

The introduction of GGBFS resulted in an adverse effect on shrinkage, with values of more than 6.3 ± 0.5 mm/m at 28 days (Fig. 4C). Such significant early-age drying shrinkage when introducing Ca-rich slag is in line with previous investigations on alkali-activated GGBFS and Fe, Ca-rich slags [19,41]. The heat-cured 0-2MPL-15G-H samples had a reduced shrinkage of more than half of the ambient-cured ones, from 6.3 ± 0.5 mm/m to 2.7 ± 0.1 mm/m. Heat curing results in a stronger binder, which provides a higher resistance to internal stress and visco-elastic deformation. The addition of 3 wt% 2MPL in the ambient-cured mortar (3-2MPL-15G-A) resulted in a shrinkage decrease of 65% (2.2 ± 0.3 mm/m). *Bílek* et al. *(2016)* reported that 1 wt % of 2MPL resulted in a major decrease in shrinkage of 80% for alkali-activated GGBFS mortars [40], but such low values were not reached in the IP mortars developed herein. 3-2MPL-15G-H mortars that underwent heat curing presented 28 days shrinkage values (2.1 ± 0.2 mm/m) that falls within the standard deviation of the shrinkage results of 3-2MPL-15G-A and both can be considered similar. The largest fraction of weight loss in 0-2MPL-15G-A occurred during the initial 7 days of the measurement (Fig. 4D) following a similar trend as the shrinkage behaviour. The weight loss of 0-2MPL-15G-A reached around 4.5% after 28 days, which is similar to the weight loss observed for 3-2MPL-15G-A

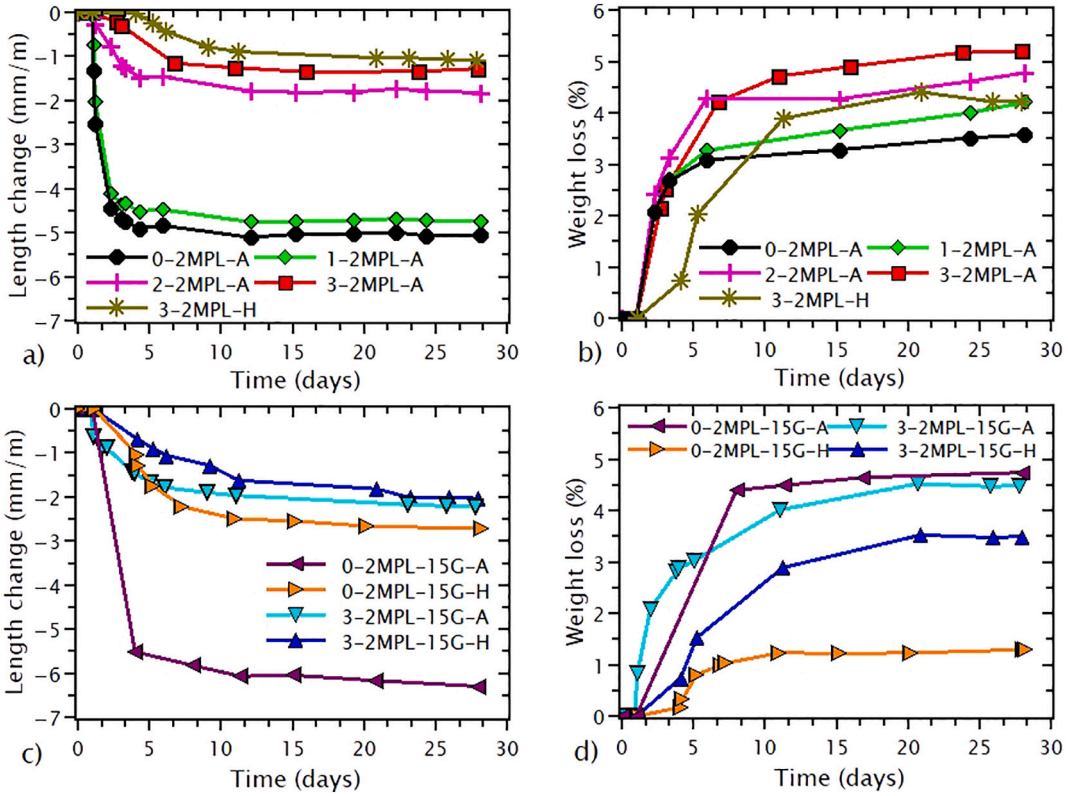

Fig. 4. Panel (a) the length change and (b) the weight loss of 0-2MPL-A, 1-2MPL-A, 2-2MPL-A, 3-2MPL-A and 3-2MPL-H. Panel (c) the length change and (d) the weight loss of 0-2MPL-15G-A, 0-2MPL-15G-H, 3-2MPL-15G-A and 3-2MPL-15G-H.

(4.7%). However, 0-2MPL-15G-H shows a significant decrease in weight loss due to heat curing being only 1.3% after 28 days, while introducing 3 wt% of 2MPL (3-2MPL-15G-H) resulted in weight loss increase from 1.3 to 3.5%. The samples 3-2MPL-H and 3-2MPL-15G-H exhibited some weight loss during heat curing (<0.7 wt%) as some water might be lost by diffusion through the plastic foil, but it is considered insignificant. The combination of GGBFS addition and heat curing (0-2MPL-15G-H) might lead to the formation of a different binder with more water uptake into the binder and the formation of closed water saturated pores, both might contribute to the decrease in weight loss.

The weight loss and length change of each sample is plotted in Fig. 5A and B, which have the purpose to determine the correlations or responsiveness of shrinkage to weight loss, identified as the slope of the curve, and to indicate the porosity [41]. Two groups of curves can be identified in Fig. 5A and three groups of curves in Fig. 5B. The two group of curves in Fig. 5A, from which a steep curve is seen for 0-2MPL-A and 1-2MPL-A, imply a high responsiveness, while 2-2MPL-A and 3-2MPL-A have a more gradual curve, implying low responsiveness. The effect of the 2MPL on the responsiveness supports that the increase in weight loss is not directly related to shrinkage but related to the pore size distribution [41], or to the sensitivity to drying rate [23]. This is different from OPC based mortars, which showed a strong correlation between moisture loss and shrinkage [23]. The low responsiveness indicate that 2-2MPL-A and 3-2MPL-A consisted of a coarser pore structure, resulting in a higher weight loss.

Mortar samples 0-2MPL-A, 0-2MPL-15G-A and 0-2MPL-15G-H presented the highest slope in Fig. 5B indicating a stronger responsiveness of shrinkage to weight loss, which is likely related to the low porosity [41]. Heat-cured samples 3-2MPL-H, 0-2MPL-15G-H and 3-2MPL-15G-H showed a similar shrinkage – weight loss relation compared to the

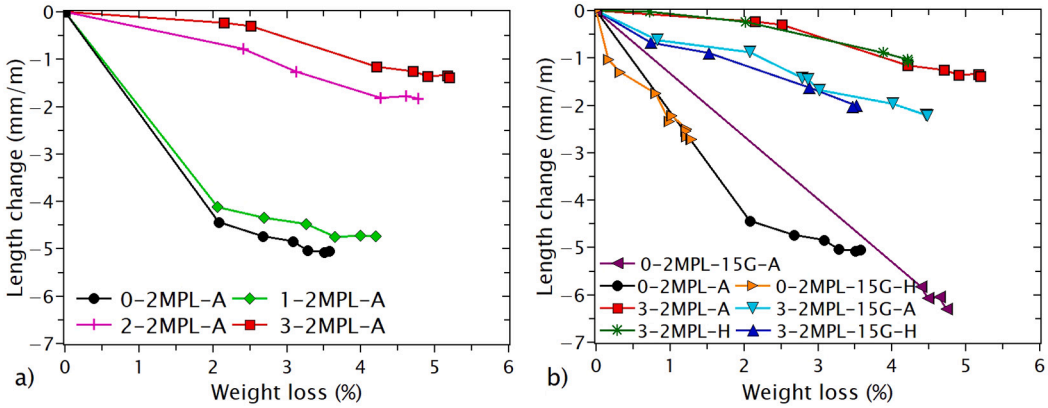

Fig. 5. The weigth loss-length change correlation for: (a) samples 0-2MPL-A, 1-2MPL-A, 2-2MPL-A and 3-2MPL-A and (b) samples 0-2MPL-A, 3-2MPL-A, 3-2MPL-H, 0-2MPL-15G-A, 0-2MPL-15G-H, 3-2MPL-15G-A and 3-2MPL-15G-H.

ambient-cured counterparts, but lower in absolute values, indicating that the pore size distribution is the same but the amount of pores might be decreased for the heat-cured ones. Apart from the shrinkage reduction due to the formation of a stronger binder upon heat curing, the heat-cured sample also exhibited a smaller weight loss due to a lower availability of water to evaporate [53]. The introduction of GGBFS clearly affected the responsiveness behaviour of the IP mortars with 2MPL (3-2MPL-15G-A and 3-2MPL-15G-H) compared to its GGBFS free counterparts, due to the change in binder products [5]. The weight loss and drying shrinkage of the studied IP mortars appeared to be higher than alkali-activated GGBFS and OPC-based mortars reported by *Ye* et al. (2017) [23], which can be explained by the lack of hydration reactions in the IP mortars resulting in a significant amount of residual water, situated in pores, which can be evaporated and form capillary stresses.

3.5. Porosity and pore size distribution

Table 4 shows the 28 days bulk density and apparent porosity determined by water absorption, and the total porosity and volume intrusion measured by MIP. MIP shows systematic higher porosity values compared to water absorption, but a similar trend can be observed for both techniques. The difference in porosity can be explained by the fact that water under vacuum can only move into pores larger than 100 nm [54], while MIP can intrude mercury, at high pressure, in pores that have a size of 5 nm. However, when analysing the MIP results, it should be taken into account that MIP measures not exactly the pore size but the size of the entrance to the pore, called pore throat. Additionally, MIP is subjected to many assumptions, and does not take into account the true tortuosity of the connections between the pore and the pore shape [55]. The total porosity and density ranged from 23% and 2.4 g/cm^3, respectively, for the most porous samples (3-2MPL-15G-H and 3-2MPL-H), to 8% and 2.6 g/cm^3, respectively, for the densest samples (0-2MPL-A and 0-2MPL-15G-A). Further, there is no significant difference in total porosity between ambient and heat-cured samples. The addition of 2MPL increased the porosity significantly and likely increased the error of the obtained apparent porosity, in particular when the tested samples were limited in size (2x2x2 cm^3). This might explain the high apparent porosity of 3-2MPL-H compared to 3-2MPL-A. A clear explanation for the high apparent porosity of sample 3-2MPL-H cannot be given and this phenomena should be further investigated.

Fig. 6A shows that in SL-based IPs (0-2MPL-A, 0-2MPL-H and 3-2MPL-A) hardly any mesopores were measured, while introducing GGBFS (0-2MPL-15G-A and 0-2MPL-15G-H) modified the binder structure promoting slightly higher mesoporosity in the region from 5 to 10 nm. The addition of 2MPL (3-2MPL-15G-A and 3-2MPL-15G-H) further increased the volume of mesopores. The mesoporous region (part of the capillary pore region) can have an impact on the shrinkage although their fraction is small in this study, only a few percent of the total cumulative pore volume (Fig. 6B). Collins and Sanjayan (2000) found that alkali-activated GGBFS mortar consisted of a larger amount of mesopores (82%) compared to OPC (36%), resulting in a higher drying shrinkage for the alkali-activated GGBFS mortars [18]. However, for Fe-rich IPs, the main pore size distribution is situated in the macropore region and is thus different from the reported alkali-activated GGBFS because of the different reaction products [18,19].

Table 4
The bulk density, total apparent porosity by water absorption and MIP, and the intruded to total volume ratio of each sample.

Sample	Bulk density (g/cm^3)	Total apparent porosity (%) by H_2O absorption	Total porosity (%) by MIP
0-2MPL-A	2.6	6.3	10.4
3-2MPL-A	2.4	10.5	20.5
3-2MPL-H	2.3	16.1	18.3
0-2MPL-15G-A	2.5	6.1	7.5
0-2MPL-15G-H	2.6	5.8	8.7
3-2MPL-15G-A	2.4	7.9	21.3
3-2MPL-15G-H	2.5	9.1	23.7

All samples showed a major increase in pore volume in the macropore region, between 0.3 and 3 μm. A shift in pore size distribution in the macropore region can be seen when GGBFS and/or 2MPL is introduced (Fig. 6A). A shift in pore size distribution towards smaller pores was measured for samples 02-MPL-A, 0-2MPL-15G-A and 0-2MPL-15G-H, followed by samples 3-2MPL-15G-A and 3-2MPL-15G-H, while shift towards larger pores was given for samples 3-2MPL-A and 3-2MPL-H. Apart from 0-2MPL-15G-A and 0-2MPL-15G-H, heat and ambient-cured samples consisted of overlapping pore size distributions. This overlap results in similar porosity values (Table 4), which points to the likelihood that the binder structure is the same. Literature reported that a finer pore structure can be formed due to the increased reactivity by heat curing [56]. The latter can be applicable for 0-2MPL-15G-H, but not for the 2MPL heat-cured samples, implying that the addition of 2MPL is the dominant factor in defining the pore size distribution. IP mortar 0-2MPL-15G-A shows a narrow pore size distribution and the lowest cumulative volume compared to all other samples, indicating a pore refinement due to the addition of GGBFS. This pore refinement might explain the large autogenous shrinkage for IPs with GGBFS (Fig. 3B). Fig. 6B shows that the cumulative volume is significantly increased when 2MPL was introduced. This increase is situated around 1 μm pore diameter, indicating that not only the pore size increased but also more pores of such diameter were formed. Consequently the capillary pore pressure was decreased significantly, resulting in a decrease in shrinkage (Fig. 4A). Logically, large pores favour the evaporation of water as shown in Fig. 4B.

The average pore size, which is 50% of the cumulative pore volume, is plotted for each sample in Fig. 6C and three different groups can be differentiated, which are the same groups as in Fig. 5B. The first group of samples, 0-2MPL-A, 0-2MPL-15G-A and 0-2MPL-15G-H, has an average pore diameter of around 0.4 μm. The second group, comprising 3-2MPL-15G-A and 3-2MPL-15G-H, has a slightly higher average pore size of 0.6 μm. The third group, consisting of 3-2MPL-A and 3-2MPL-H, has an average pore size diameter of 0.8 μm. 2MPL is reported to act as a surfactant in OPC-based systems [57], and thus has the ability to entrain air [58], resulting in the formation of more and larger pores, and a shift in pore size. Probably, 2MPL is also effective as a surfactant in IP systems, as its addition shifted the pore size distribution to larger pores. Different surfactants were used in IP systems before, but with the aim to produce porous IPs and not in an attempt to increase the volumetric stability [59].

3.6. Scanning electron microscopy (SEM)

A significant amount of cracks was identified in the matrix of 0-2MPL-15G-A originating from voids or from the center of large areas of binder, which is probably the result of high shrinkage (Fig. 7A). The presence of cracks can also explain the high weight loss of 0-2MPL-15G-A, as more surface was made available for drying. The crack branches showed a typical Y-shape [60], due to stress initiated from drying, and the crack propagation appeared to end at the sand grains. Expectedly, no macrocracks were visible in the IP mortar with 2MPL, as shown for sample 3-2MPL-15G-A in Fig. 7B and 3-2MPL-A in Fig. 7C. Samples 3-2MPL-15G-A and 3-2MPL-A clearly show the presence of spherical pores (ranging from 5 to 76 μm diameter) in the matrix (Fig. 7C), which agrees with the measured increase in porosity and with the fact that 2MPL acts as an air entrainer. The presence of large pores and absence of cracks indicate that a large capillary stress was likely not buildup during drying in samples with 2MPL. The microstructure of 3-2MPL-A is shown in Fig. 7C where quartz sand, unreacted Fe-rich slag particles (SL), metallic Fe particles and IP binder were identified. Three distinct zones

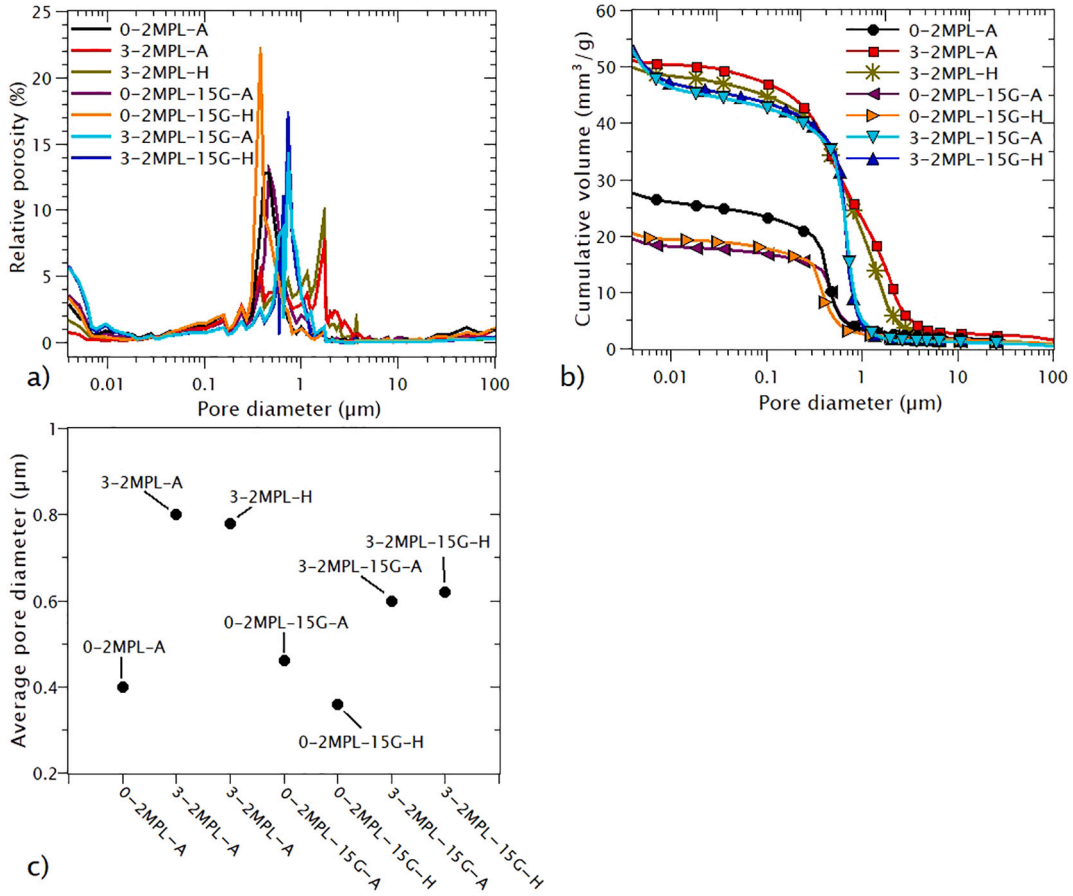

Fig. 6. The pore size distribution of 0-2MPL-A, 3-2MPL-A, 3-2MPL-H, 0-2MPL-15G-A, 0-2MPL-15G-H, 3-2MPL-15G-A and 3-2MPL-15G-H: (a) the relative porosity (%) for each pore diameter (μm); (b) the cumulative volume (mm^3/g) with pore diameter (μm) and (c) the average pore diameter.

were identified (indicated in Fig. 7D) in the vicinity of a metallic Fe particle (originating from SL), in which the first zone is the metallic Fe particle, often surrounded by a second zone of light grey crystalline phases. The crystalline phases remained unreacted and were identified as spinel solid solutions, which were surrounded by unreacted amorphous Fe-rich glass of SL. The third zone was composed of small particles of unreacted amorphous Fe-rich glass and spinels enclosed by the binder.

EDX point analyses showed that the binder is mainly composed of Fe, Si and Al, elements originating from the slag, as well as K and Si, originating from the activating solution (Fig. 7E). The binder that was formed is most likely a complex K-(Fe,Al)-Si-(H) binder, which is in a way comparable to the typical K-A-S-H binder, formed from an alkali-activated aluminosilicate precursor [14,61,62]. The Fe^{3+} is situated in a 4-fold coordination in the silicate network of the IP binder, in a similar way as the 4-fold coordinated Al^{3+} in geopolymers [51]. The total Fe content of SL consisted of 4.9 wt% of Fe^{3+} and 69.5 wt% of Fe^{2+}, which might indicate that not only an Fe^{3+} binder is formed, but also Fe^{2+} trioctahedral layers.

Elemental point analysis showed that in 0-2MPL-15G-A and 3-2MPL-15G-A the binder around the GGBFS particles is more enriched in Ca, which proves that a different binder is formed which can lead to a different pores size distribution (Fig. 8). The enrichment in Ca demonstrated that a C-A-S-H type of binder was initially formed around the GGBFS particles [63]. In this way, the reaction of the SL and the metallic Fe is hindered as it is covered by the early formed binder, inhibiting oxidation and consequently expansion did not take place. It is possible that with time Fe^{2+} from SL can dissolve and oxidise to Fe^{3+} and can, via diffusion, be incorporated into the initial C-A-S-H type of binder [64], resulting in the presence of Fe in the binder, which was confirmed by elemental point analysis.

3.7. Mechanical strength

The 28 day flexural and compressive strength of the IP mortars are shown in Fig. 9A and B. The compressive strength of 0-2MPL-A mortars, with an average value of 48.8 ± 0.8 MPa, is not significantly modified by the addition of 2MPL dosages up to 2 wt% (1-2MPL-A and 2-2MPL-A). At higher 2MPL dosages (3 wt%, 3-2MPL-A) a small decrease of 5% in average compressive strength (46.4 ± 5.6 MPa) was observed, along with a higher standard deviation. A higher standard deviation can be attributed to the increased porosity in the samples [65]. Heat-curing increased the compressive strength by 45%, up to 67.3 ± 3.3 MPa for 3-2MPL-H, which can be explained by accelerated reaction kinetics and the development of a stronger binder [66].

The addition of 15 wt% GGBFS (0-2MPL-15G-A) decreased the compressive strength considerably, from 48.8 ± 0.8 MPa to 34.1 ± 1.3 MPa. The low mechanical strength of 0-2MPL-15G-A can be explained by the increased reactivity at early age and fast precipitation of a different binder. When this binding (0-2MPL-15G-A) was exposed to drying, a pronounced shrinkage occurred and numerous cracks were formed, as shown in Fig. 7A, which negatively affected the mechanical properties. Heat curing increased the compressive strength to 99.4 ± 3.4 MPa (0-2MPL-15G-H). 3-2MPL-15G-A had a compressive strength of 64.8 ± 3.8 MPa, which is almost twice the strength of its 2MPL-free counterparts (0-2MPL-15G-A, 34.1 ± 1.3 MPa). The increase in strength for 3-2MPL-15G-A can be related to significant decrease in shrinkage, and consequently an expected reduction in the amount of cracks. The 3-2MPL-15G-H mortars showed a compressive strength of 86.9 ± 3.2 MPa, which is higher compared to 3-2MPL-15G-A (64.8 ±

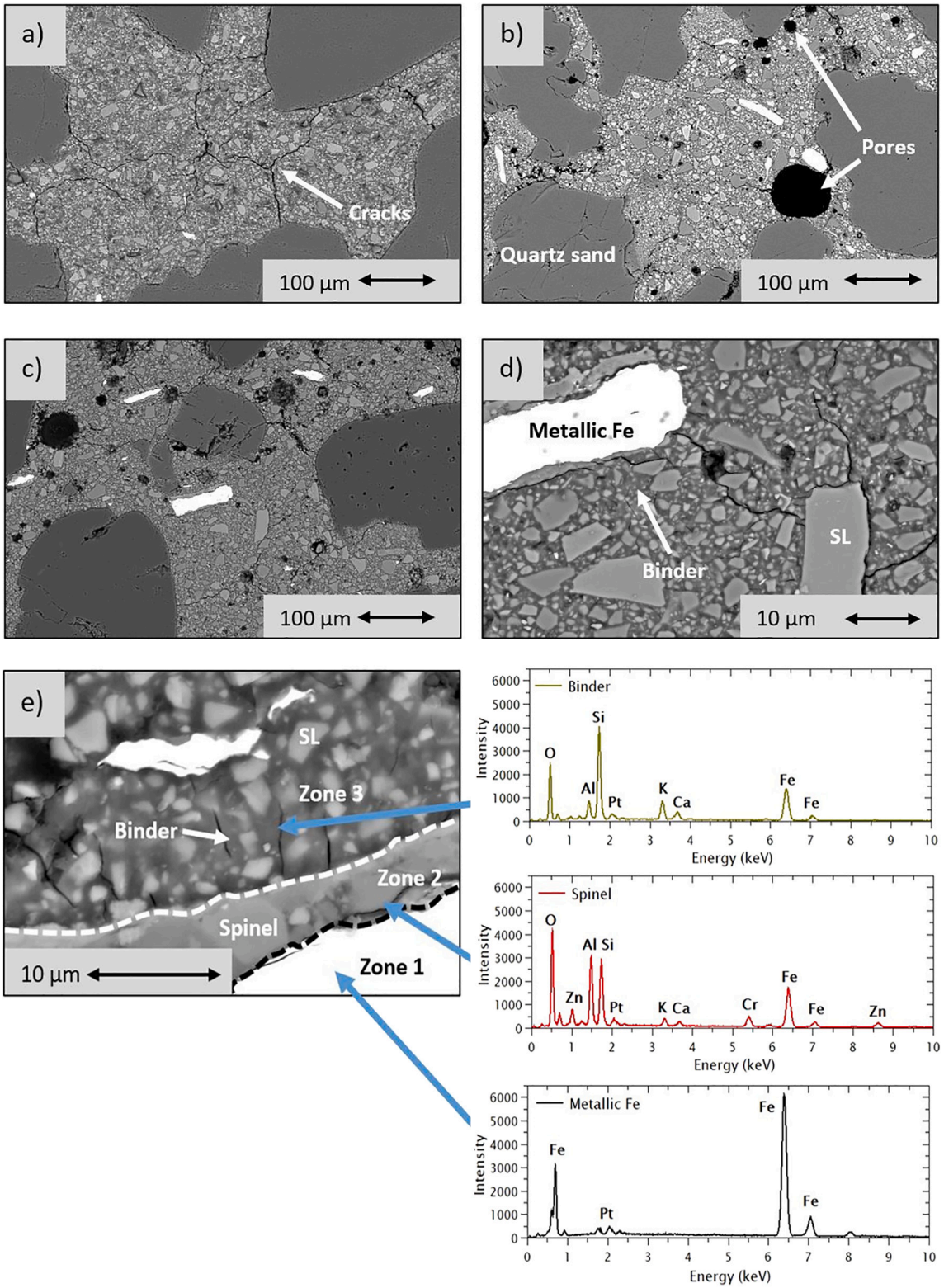

Fig. 7. The microstructure: (a) of 0-2MPL-15G-A; (b) of 3-2MPL-15G-A; (c) of 3-2MPL-A; all three at magnification 200. Panels (d) and (e) the microstructure of 3-2MPL-A at magnification 1000 and 3500, respectively, along with qualitative chemical point analysis.

3.8 MPa). When heat curing was performed, 3-2MPL-15G-H could not reach similar compressive strength as 0-2MPL-15G-H (99.4 ± 3.4 MPa), which can be related to the higher porosity in 3-2MPL-15G-H that can negatively affect strength [65].

The 0-2MPL-A and 1-2MPL-A mortars showed a similar flexural strength of 3.7 ± 0.3 MPa (Fig. 9B). When adding 2 or 3 wt% 2MPL (2-2MPL-A and 3-2MPL-A), however, flexural strength increased significant by 89%, up to 7.0 ± 0.9 MPa and can be, upon heat curing (3-2MPL-H), further increased up to 9.0 ± 0.5 MPa. The addition of 2MPL in GGBFS containing mortars (3-2MPL-15G-A) resulted in a flexural strength increase from 2.3 ± 0.1 MPa to 6.2 ± 2.2 MPa. Heat cured samples 0-2MPL-15G-H and 3-2MPL-15G-H showed a flexural strength

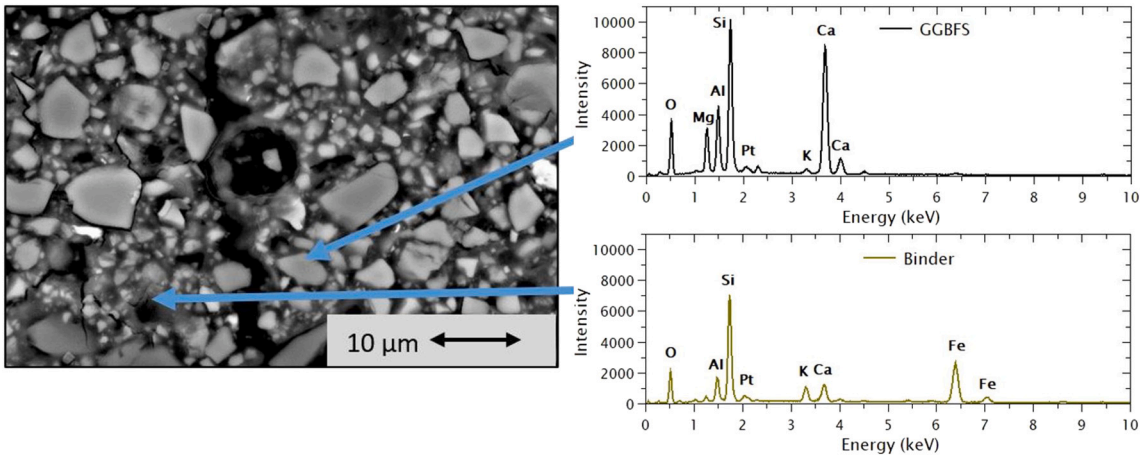

Fig. 8. The microstructure of 3-2MPL-15G-A. Included are the chemical point analysis to identify the GGBFS chemistry (top right figure) and binder (bottom right figure).

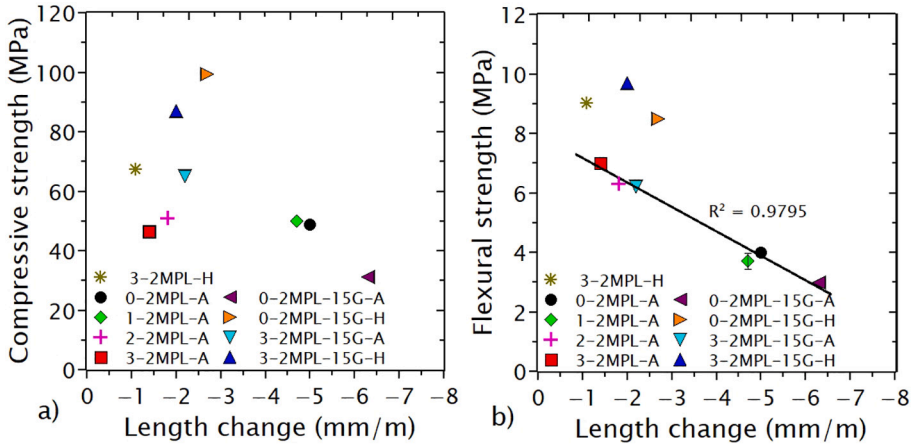

Fig. 9. The 28 day strength - drying shrinkage correlation for each sample: (a) compressive strength and drying shrinkage; (b) flexural strength and drying shrinkage.

of 8.5 ± 0.1 MPa and 9.7 ± 1.0 MPa, respectively, which is increased compared to its ambient-cured counterparts 0-2MPL-15G-A and 3-2MPL-15G-A. In general, the flexural strength appeared to be dependent on the amount of shrinkage as mortars with the highest shrinkage values presented the lowest flexural strength. A regression analysis was performed on the data of all ambient-cured samples in Fig. 9B, resulting in a R^2-value of 0.98, suggesting that there is a correlation between flexural strength and shrinkage [12].

4. Conclusions

This paper investigated the volumetric stability of IP mortars formed upon alkali activation of a metallurgical Fe-rich slag. The volumetric stability was identified and increased by modifying the pore size distribution. The pore size distribution was modified by exploring different strategies such as the introduction of SRA 2-methyl-2,4-pentanediol (2MPL), GGBFS and by applying heat curing.

The autogenous shrinkage of Fe-rich IP mortar was found to be low (0.7 mm/m), however, a significant expansion event occurred during hardening which can result in curling or cracks. This expansion might be related to the oxidation of metallic Fe and/or the formation of Fe^{2+} trioctahedral layers. Fe-rich IP mortars exhibited drying shrinkage (5.1 mm/m) which is significant due to the lack of hydration reactions and a pore size distribution which was mainly (>80%) situated in the capillary macropore region (0.1–3 µm).

The introduction of more than 2 wt% 2MPL, which acted as an air entrainer, resulted in a shift in pore size distribution to larger pore sizes without a loss of compressive strength (>45.0 MPa) and consequently reduced the shrinkage (1.8 mm/m). A correlation between drying shrinkage and flexural strength can be made, as the flexural strength increased when the drying shrinkage was decreased.

The drying shrinkage (6.3 mm/m) increased when GGBFS was introduced in the IP mortar and extensive crack formation was observed, which negatively affected the compressive strength (34.1 MPa).

Heat curing increased mechanical strength and enabled the accommodation of higher capillary stress. In this way, the drying shrinkage decreased by 57% and fewer cracks were formed. Heat curing in combination with 2MPL was shown to be ineffective for further shrinkage reduction, as 2MPL overrode the effect of heat curing.

This research bridged the gap in literature with respect to the volumetric stability of Fe-rich IPs and showed that the shrinkage is driven by the pore size distribution. The addition of 2MPL was proven to be effective in lowering the shrinkage considerably without compromising mechanical strength. This research takes a step towards solving an important issue of IPs from Fe-rich slags (i.e. shrinkage), which so far can be considered as a barrier for a wider industrial implementation as a potential binder for construction materials.

CRediT authorship contribution statement

Glenn Beersaerts: Conceptualization, Methodology, Investigation, Writing-Original Draft, Writing – Review and Editing, Visualization.

Guilherme Ascensão: Methodology, Investigation, Writing – Review and Editing. Yiannis Pontikes: Supervision, Writing – Review and Editing.

Declaration of competing interest

The authors declare that they have no known competing financial interests or personal relationships that could have appeared to influence the work reported in this paper.

Acknowledgements

The authors would like to thank M. Giels and T. Hertel for the interesting discussions and their assistance when performing mechanical tests. The authors would like to thank the Center for Resource, Recovery and Recycling (CR3) for funding this research (https://wp.wpi.edu/cr3/). G. Ascensão has received funding from the European Union's Horizon 2020 research and innovation programme under the Marie Skłodowska-Curie grant agreement No 721185. The authors declare that there is no conflict of interest regarding the publication of this article.

References

[1] R. Snellings, Assessing, understanding and unlocking supplementary cementitious materials, RILEM Tech. Lett. 1 (2016) 50, https://doi.org/10.21809/rilemtechlett.2016.12.
[2] B. Gorai, R.K. Jana, Premchand, Characteristics and utilisation of copper slag—a review, Res., Conser. Recycl. 39 (2003) 299–313, https://doi.org/10.1016/S0921-3449(02)00171-4.
[3] C. Morrison, R. Hooper, K. Lardner, The use of ferro-silicate slag from ISF zinc production as a sand replacement in concrete, Cem. Concr. Res. 33 (2003) 2085–2089, https://doi.org/10.1016/S0008-8846(03)00234-5.
[4] Y. Pontikes, L. Machiels, S. Onisei, L. Pandelaers, D. Geysen, P.T. Jones, B. Blanpain, Slags with a high Al and Fe content as precursors for inorganic polymers, App. Clay Sci. 73 (2013) 93–102, https://doi.org/10.1016/j.clay.2012.09.020.
[5] P. Duxson, A. Fernández-Jiménez, J.L. Provis, G.C. Lukey, A. Palomo, J.S.J. van Deventer, Geopolymer technology: the current state of the art, J. Mater. Sci. 42 (2007) 2917–2933, https://doi.org/10.1007/s10853-006-0637-z.
[6] S. Onisei, K. Lesage, B. Blanpain, Y. Pontikes, Early age microstructural transformations of an inorganic polymer made of fayalite slag, J. Am. Ceram. Soc. 98 (2015) 2269–2277, https://doi.org/10.1111/jace.13548.
[7] L.K. Turner, F.G. Collins, Carbon dioxide equivalent (CO2-e) emissions: a comparison between geopolymer and OPC cement concrete, Constr. Build. Mater. 43 (2013) 125–130, https://doi.org/10.1016/j.conbuildmat.2013.01.023.
[8] L. Kriskova, L. Machiels, Y. Pontikes, Inorganic polymers from a plasma convertor slag: effect of activating solution on microstructure and properties, J. Sustain. Metall. 1 (2015) 240–251, https://doi.org/10.1007/s40831-015-0022-8.
[9] L. Machiels, L. Arnout, P. Yan, P.T. Jones, B. Blanpain, Y. Pontikes, Transforming enhanced landfill mining derived gasification/vitrification glass into low-carbon inorganic polymer binders and building products, J. Sustain. Metall. 3 (2017) 405–415, https://doi.org/10.1007/s40831-016-0105-1.
[10] R.I. Iacobescu, V. Cappuyns, T. Geens, L. Kriskova, S. Onisei, P.T. Jones, Y. Pontikes, The influence of curing conditions on the mechanical properties and leaching of inorganic polymers made of fayalitic slag, Front. Chem. Sci. Eng. 11 (2017) 317–327, https://doi.org/10.1007/s11705-017-1622-6.
[11] L. Machiels, L. Arnout, P.T. Jones, B. Blanpain, Y. Pontikes, Inorganic polymer cement from Fe-silicate glasses: varying the activating solution to glass ratio, Waste Biomass Valor. 5 (2014) 411–428, https://doi.org/10.1007/s12649-014-9296-5.
[12] C. Kuenzel, L.J. Vandeperre, S. Donatello, A.R. Boccaccini, C. Cheeseman, Ambient temperature drying shrinkage and cracking in metakaolin-based geopolymers, J. Am. Ceram. Soc. 95 (2012) 3270–3277, https://doi.org/10.1111/j.1551-2916.2012.05380.x.
[13] F. Collins, J. Sanjayan, Cracking tendency of alkali-activated slag concrete subjected to restrained shrinkage, Cem. Concr. Res. 30 (2000) 791–798, https://doi.org/10.1016/S0008-8846(00)00243-X.
[14] F. Pacheco-Torgal, J. Labrincha, C. Leonelli, A. Palomo, P. Chindaprasirt (Eds.), Handbook of Alkali-Activated Cements, Mortars and Concretes, Woodhead Publishing, Cambridge, Philadelphia, PA, 2012.
[15] O.M. Jensen, P.F. Hansen, Autogenous deformation and RH-change in perspective, Cem. Concr. Res. 31 (2001) 1859–1865, https://doi.org/10.1016/S0008-8846(01)00501-4.
[16] A.A. Melo Neto, M.A. Cincotto, W. Repette, Drying and autogenous shrinkage of pastes and mortars with activated slag cement, Cem. Concr. Res. 38 (2008) 565–574, https://doi.org/10.1016/j.cemconres.2007.11.002.
[17] F.H. Wittmann, On the action of capillary pressure in fresh concrete, Cem. Concr. Res. 6 (1976) 49–56, https://doi.org/10.1016/0008-8846(76)90050-8.
[18] F. Collins, J. Sanjayan, Effect of pore size distribution on drying shrinkage of alkali-activated slag concrete, Cem. Concr. Res. 30 (2000) 1401–1406, https://doi.org/10.1016/S0008-8846(00)00327-6.
[19] G. Ascensão, G. Beersaerts, M. Marchi, M. Segata, F. Faleschini, Y. Pontikes, Shrinkage and mitigation strategies to improve the dimensional stability of CaO-FeOx-Al2O3-SiO2 inorganic polymers, Materials 12 (2019) 1–20, https://doi.org/10.3390/ma12223679.
[20] G. Ascensão, M. Marchi, M. Segata, F. Flora, Y. Pontikes, Increasing the dimensional stability of CaO-FeOx-Al2O3-SiO2 alkali-activated materials: A study on the swelling potential of calcium oxide-rich admixtures, Detritus J. 8 (2019) 91–100, https://doi.org/10.31025/2611-4135/2019.13880.
[21] N.K. Lee, J.G. Jang, H.K. Lee, Shrinkage characteristics of alkali-activated fly ash/slag paste and mortar at early ages, Cem. Concr. Res. 53 (2014) 239–248, https://doi.org/10.1016/j.cemconcomp.2014.07.007.
[22] J.L. Provis, J.S.J. van Deventer, Alkali Activated Materials: State of the Art, Springer Netherlands, Dordrecht, 2014.
[23] H. Ye, C. Cartwright, F. Rajabipour, A. Radlińska, Understanding the drying shrinkage performance of alkali-activated slag mortars, Cem. Concr. Compos. 76 (2017) 13–24, https://doi.org/10.1016/j.cemconcomp.2016.11.010.
[24] D.H. Everett, Manual of Symbols and Terminology for Physicochemical Quantities and Units: Appendix II, Definitions, Terminology and Symbols in Colloid and Surface Chemistry, Part I, Colloid and Surface Chemistry, Washington DC, USA, 2001.
[25] S. Mindess, J.F. Young, D. Darwin, Concrete, 2nd ed., Prentice Hall, Upper Saddle River, NJ, 2003.
[26] D. Ballekere Kumarappa, S. Peethamparan, M. Ngami, Autogenous shrinkage of alkali activated slag mortars: basic mechanisms and mitigation methods, Cem. Concr. Res. 109 (2018) 1–9, https://doi.org/10.1016/j.cemconres.2018.04.004.
[27] H. Ye, A. Radlińska, Shrinkage mechanisms of alkali-activated slag, Cem. Conc. Res. 88 (2016) 126–135, https://doi.org/10.1016/j.cemconres.2016.07.001.
[28] Z. Li, M. Nedeljković, B. Chen, G. Ye, Mitigating the autogenous shrinkage of alkali-activated slag by metakaolin, Cem. Concr. Res. 122 (2019) 30–41, https://doi.org/10.1016/j.cemconres.2019.04.016.
[29] T. Bakharev, J. Sanjayan, Y.-B. Cheng, Effect of admixtures on properties of alkali-activated slag concrete, Cem. Concr. Res. 30 (2000) 1367–1374, https://doi.org/10.1016/S0008-8846(00)00349-5.
[30] X. Yuan, W. Chen, Z. Lu, H. Chen, Shrinkage compensation of alkali-activated slag concrete and microstructural analysis, Constr. Build. Mater. 66 (2014) 422–428, https://doi.org/10.1016/j.conbuildmat.2014.05.085.
[31] Z. Li, W. Zhang, R. Wang, F. Chen, X. Jia, P. Cong, Effects of reactive MgO on the reaction process of geopolymer, Materials 12 (2019) 1–10, https://doi.org/10.3390/ma12030526.
[32] W. Chen, H. Brouwers, Hydration of mineral shrinkage-compensating admixture for concrete: an experimental and numerical study, Constr. Build. Mater. 26 (2012) 670–676, https://doi.org/10.1016/j.conbuildmat.2011.06.070.
[33] L. Coppola, D. Coffetti, E. Crotti, S. Candamano, F. Crea, G. Gazzaniga, T. Pastore, The combined use of admixtures for shrinkage reduction in one-part alkali activated slag-based mortars and pastes, Constr. Build. Mater. 248 (2020) 118682, https://doi.org/10.1016/j.conbuildmat.2020.118682.
[34] M. Palacios, F. Puertas, Effect of shrinkage-reducing admixtures on the properties of alkali-activated slag mortars and pastes, Cem. Concr. Res. 37 (2007) 691–702, https://doi.org/10.1016/j.cemconres.2006.11.021.
[35] M. Palacios, F. Puertas, Estabilidad de aditivos superplastificantes y reductores de la retracción en medios fuertemente básicos, Mater. Construcc. 54 (2004) 65–86, https://doi.org/10.3989/mc.2004.v54.i276.256.
[36] O. Mikhailova, P. Rovnaník, Stability of polymer admixtures in alkaline media, Mater. Sci. Forum 908 (2017) 145–153, https://doi.org/10.4028/www.scientific.net/MSF.908.145.
[37] M. Palacios, Y.F. Houst, P. Bowen, F. Puertas, Adsorption of superplasticizer admixtures on alkali-activated slag pastes, Cem. Concr. Res. 39 (2009) 670–677, https://doi.org/10.1016/j.cemconres.2009.05.005.
[38] L. Kalina, V. Bílek, E. Bartoníčková, J. Krouská, Polypropylene glycols as effective shrinkage-reducing admixtures in alkali-activated materials, ACI Mater. J. 115 (2018) 251–256, https://doi.org/10.14359/51701099.
[39] V. Bílek, L. Kalina, R. Novotný, Polyethylene glycol molecular weight as an important parameter affecting drying shrinkage and hydration of alkali-activated slag mortars and pastes, Constr. Build. Mater. 166 (2018) 564–571, https://doi.org/10.1016/j.conbuildmat.2018.01.176.
[40] V. Bílek, L. Kalina, R. Novotný, J. Tkacz, L. Pařízek, Some issues of shrinkage-reducing admixtures application in alkali-activated slag systems, Materials 9 (2016), https://doi.org/10.3390/ma9060462.
[41] R.J. Thomas, D. Lezama, S. Peethamparan, On drying shrinkage in alkali-activated concrete: improving dimensional stability by aging or heat-curing, Cem. Concr. Res. 91 (2017) 13–23, https://doi.org/10.1016/j.cemconres.2016.10.003.
[42] H. Ye, A. Radlinska, Shrinkage mitigation strategies in alkali-activated slag, Cem. Concr. Res. 101 (2017) 131–143, https://doi.org/10.1016/j.cemconres.2017.08.025.
[43] P. Close, H.M. Sherpherd, C.H. Drummond, Determination of several valences of iron, arsenic and antimony, and selenium in glass, J. Am. Ceram. Soc. 41 (1958) 455–460.
[44] C09 Committee, Test Method for Autogenous Strain of Cement Paste and Mortar, ASTM International, West Conshohocken, PA 91.100.10.
[45] BS EN 1936, Natural Stone Test Methods. Determination of Real Density and Apparent Density, and of Total and Open Porosity, BSI 73.020, 2007, 2006.
[46] A. Zingg, F. Winnefeld, L. Holzer, J. Pakusch, S. Becker, R. Figi, L. Gauckler, Interaction of polycarboxylate-based superplasticizers with cements containing

different C3A amounts, Cem. Concr. Compos. 31 (2009) 153–162, https://doi.org/10.1016/j.cemconcomp.2009.01.005.
[47] E. Deir, B.S. Gebregziabiher, S. Peethamparan, Influence of starting material on the early age hydration kinetics, microstructure and composition of binding gel in alkali activated binder systems, Cem. Concr. Compos. 48 (2014) 108–117, https://doi.org/10.1016/j.cemconcomp.2013.11.010.
[48] R. Snellings, Solution-controlled dissolution of supplementary cementitious material glasses at pH 13: the effect of solution composition on glass dissolution rates, J. Am. Ceram. Soc. 96 (2013) 2467–2475, https://doi.org/10.1111/jace.12480.
[49] X. Gao, Q.L. Yu, H. Brouwers, Reaction kinetics, gel character and strength of ambient temperature cured alkali activated slag–fly ash blends, Constr. Build. Mater. 80 (2015) 105–115, https://doi.org/10.1016/j.conbuildmat.2015.01.065.
[50] E.E. Holt, Early Age Autogenous Shrinkage of Concrete, Technical Research Centre of Finland, Espoo, 2001.
[51] A. Peys, A.P. Douvalis, V. Hallet, H. Rahier, B. Blanpain, Y. Pontikes, Inorganic polymers from CaO-FeOx-SiO2 slag: the start of oxidation of Fe and the formation of a mixed valence binder, Front. Mater. 6 (2019) 1–10, https://doi.org/10.3389/fmats.2019.00212.
[52] M.L.S. Rivetti, J.S.A. Neto, N.S.A. Júnior, D.V. Ribeiro, Chapter 2 Corrosion inhibitors for reinforced concrete, in: M. Aliofkhazraei (Ed.), Corrosion inhibitors, principles and recent applications, Intech, London, 2018, pp. 35–58.
[53] R.J. Thomas, S. Peethamparan, Alkali-activated concrete: engineering properties and stress–strain behavior, Constr. Build. Mater. 93 (2015) 49–56, https://doi.org/10.1016/j.conbuildmat.2015.04.039.
[54] K. Meyer, P. Lorenz, B. Böhl-Kuhn, P. Klobes, Porous solids and their characterization methods of investigation and application, Cryst. Res. Technol. 29 (1994) 903–930, https://doi.org/10.1002/crat.2170290702.
[55] G. Andriani, N. Walsh, Fabric, porosity and water permeability of calcarenites from Apulia (SE Italy) used as building and ornamental stone, Bull. Eng. Geol. Environ. 62 (2003) 77–84, https://doi.org/10.1007/s10064-002-0174-1.
[56] Y. Ma, J. Hu, G. Ye, The pore structure and permeability of alkali activated fly ash, Fuel 104 (2013) 771–780, https://doi.org/10.1016/j.fuel.2012.05.034.
[57] M. Ilg, J. Plank, Non-adsorbing small molecules as auxiliary dispersants for polycarboxylate superplasticizers, Colloids Surf. A Physicochem. Eng. 587 (2020) 124307, https://doi.org/10.1016/j.colsurfa.2019.124307.
[58] B. Feneuil, O. Pitois, N. Roussel, Effect of surfactants on the yield stress of cement paste, Cem. Concr. Res. 100 (2017) 32–39, https://doi.org/10.1016/j.cemconres.2017.04.015.
[59] T. Hertel, R.M. Novais, R. Murillo Alarcón, J.A. Labrincha, Y. Pontikes, Use of modified bauxite residue-based porous inorganic polymer monoliths as adsorbents of methylene blue, J. Clean. Prod. 227 (2019) 877–889, https://doi.org/10.1016/j.jclepro.2019.04.084.
[60] L. Goehring, A. Nakahara, T. Dutta, S. Kitsunezaki, S. Tarafdar, Desiccation Cracks and their Patterns: Formation and Modelling in Science and Nature, Wiley-VCH, Weinheim, Germany, 2015.
[61] A. Fernández-Jiménez, R. Vallepu, T. Terai, A. Palomo, K. Ikeda, Synthesis and thermal behavior of different aluminosilicate gels, J. Non-Cryst. Solid. 352 (2006) 2061–2066, https://doi.org/10.1016/j.jnoncrysol.2006.03.037.
[62] V. Glukhovsky, Soil Silicate Articles and Structures, Budivelnyk, Kiev, 1967.
[63] Z. Huanhai, W. Xuequan, X. Zhongzi, T. Mingshu, Kinetic study on hydration of alkali-activated slag, Cem. Concr. Res. 23 (1993) 1253–1258, https://doi.org/10.1016/0008-8846(93)90062-E.
[64] A. Mancini, E. Wieland, G. Geng, R. Dähn, J. Skibsted, B. Wehrli, B. Lothenbach, Fe (III) uptake by calcium silicate hydrates, Appl. Geochem. 113 (2020) 1–15, https://doi.org/10.1016/j.apgeochem.2019.104460.
[65] C. Shi, Strength, pore structure and permeability of alkali-activated slag mortars, Cem. Concr. Res. 26 (1996) 1789–1799, https://doi.org/10.1016/S0008-8846(96)00174-3.
[66] G. Kovalchuk, A. Fernández-Jiménez, A. Palomo, Alkali-activated fly ash: effect of thermal curing conditions on mechanical and microstructural development – part II, Fuel 86 (2007) 315–322, https://doi.org/10.1016/j.fuel.2006.07.010.